Photoinduced Hole Injection into a Self-Assembled π-Extended G-Quadruplex

Yi-Lin Wu,* Kristen E. Brown, Daniel M. Gardner, Scott M. Dyar, and Michael R. Wasielewski*

Department of Chemistry and Argonne-Northwestern Solar Energy Research (ANSER) Center, Northwestern University, Evanston, Illinois 60208-3113, United States

ⓢ *Supporting Information*

ABSTRACT: We have prepared a G-quadruplex (**GQ-1**) that incorporates an 8-(4′-aminophenylethynyl)guanine (GEAn) electron donor covalently attached to a 4-aminonaphthalene-1,8-imide (ANI) chromophore and a naphthalene-1,8:4,5-bis-(dicarboximide) (NDI) electron acceptor (GEAn-ANI-NDI, **1**). In the presence of KPF_6 in tetrahydrofuran (THF), **1** self-assembles into a monodisperse, C_4-symmetric **GQ-1** with small spatial intraquadruplex overlap between the ANI-NDI units. Photoexcitation of monomeric **1** induces the two-step charge transfer GEAn-^{1}*ANI-NDI → GEAn$^{+\bullet}$-ANI$^{-\bullet}$-NDI → GEAn$^{+\bullet}$-ANI-NDI$^{-\bullet}$ that occurs in τ_{CS1} = 5 ps and τ_{CS2} = 330 ps, respectively, while charge recombination in ca. 300 ns. Sharpening of the GEAn$^{+\bullet}$ transient absorption and a shift of the ethynyl vibrational frequency in **1** were observed, concomitant with the stepwise electron transfer from ANI$^{-\bullet}$ to NDI. Formation of **GQ-1** from **1** in THF increases the secondary charge-shifting rate (τ_{CS2} = 110 ps) and results in no change in ethynyl vibrational frequency. Charge recombination in **GQ-1** is slowed by enhanced radical-pair intersystem crossing driven by the greater number of hyperfine couplings in the assembly. Moreover, time-resolved EPR spectroscopy shows that the spin−spin-exchange interaction (J) between the radicals of GEAn$^{+\bullet}$-ANI-NDI$^{-\bullet}$ within **GQ-1** is smaller than that of **1**, suggesting that the spin (charge) density in GEAn$^{+\bullet}$ is more dispersed in **GQ-1**. The spectroscopic results are consistent with hole sharing among the guanines within the G-quadruplex that is kinetically competitive with the formation of GEAn$^{+\bullet}$. This suggests that G-quadruplexes can serve as effective hole conduits in ordered donor−acceptor assemblies.
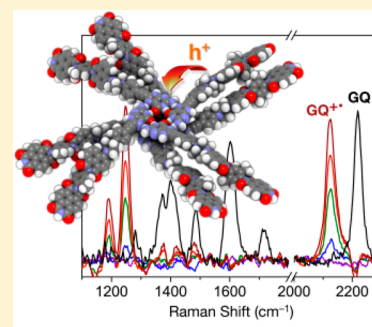
INTRODUCTION

Self-assembly of small electron donor−acceptor (D−A) molecules into discrete and monodisperse nanostructures provides geometrically defined platforms to emulate the photoinduced electron-transfer processes in photosynthetic systems,[1,2] in which highly efficient light harvesting and charge separation over a long distances are achieved by taking advantage of well-positioned chromophores.[3−5] Organization of molecules by this thermodynamically driven method can result in architectures with unique interchromophore relationships that are otherwise difficult to realize by conventional covalent synthesis. In particular, π-stacked D−A dyads and triads[6−13] can afford ordered and segregated D/A domains through which photogenerated holes and electrons can be further separated and rapidly transported to electrodes, as required in organic photovoltaics. The design of these self-ordering systems must ensure that charge hopping of the separated holes and electrons between the noncovalent donors and acceptors within their respective segregated conduits must be significantly faster than charge recombination. It has been demonstrated that photoinduced charge separation can indeed take place among noncovalently associated chromophoric redox partners with lifetimes >1 μs and enhanced photocurrents in these extended structures.[12−20] These promising results suggest that photogenerated holes and electrons may be transported independently through well-ordered, segregated molecular

charge conduits relevant to organic photovoltaics and other electronics.

We have recently exploited cation-induced guanine-quadruplexes (G-quadruplexes)[21−23] to organize molecules into a core−shell columnar architecture.[24] When functionalized with suitable electron-accepting units on the periphery, G-quadruplexes afford a segregated acceptor domain in the shell, with the electron-rich guanines hydrogen bonded and π-stacked in the core of these architectures. Furthermore, the cation-responsive nature of this system[25,26] allows for precise size control and comparisons of the photophysical properties of the monomeric and the self-assembled states. For instance, the G-quadruplex of a guanine-perylene-3,4:9,10-bis(dicarboximide) conjugate (G-PDI), where the inner column consists of the electron-rich G-quadruplex and the outer shell of PDI electron acceptors, was found to exhibit a 100-fold longer photoinduced charge separation lifetime than its monomer.[24]

While the extended charge-separation lifetime found in the G-PDI quadruplex was largely attributed to the stabilization of the radical anion between the cofacially positioned PDIs, the contribution of the core G-quadruplex to the electron-transfer dynamics remains unclear. The guanine radical cation in a tightly hydrogen-bonded G-quartet (a single layer, hydrogen-

bonded cyclic G-tetramer) and/or a G-quadruplex assembled from two or more G-quartets may be stabilized by charge delocalization relative to the monomer, a phenomenon related to the unique hole-trapping ability of G-quadruplexes.[27−29] Investigation of a G-quadruplex based on a D−A triad that displays weak anion stabilization by the neighboring acceptor units may shed light on the role of the core G-quadruplex in mediating the photoinduced electron-transfer process.

We present here a photophysical study of a new G-quadruplex (**GQ-1**) that incorporates an 8-(4′-aminophenylethynyl)guanine (GEAn) electron donor covalently attached to a 4-aminonaphthalene-1,8-imide (ANI) chromophore and a naphthalene-1,8:4,5-bis(dicarboximide) (NDI) electron acceptor (GEAn-ANI-NDI, **1**). Structurally well-defined covalent donor-ANI-NDI systems have been used to characterize photogenerated long-lived radical ion pairs (RPs) in a variety of systems.[30−32] The ethynylaniline substituent on the GEAn electron donor provides sufficient driving force for photoinitiated two-step charge separation as well as clear vibrational spectroscopic signatures to probe time-dependent structural changes. The resulting photogenerated NDI radical anion of the GEAn⁺•-ANI-NDI⁻• RP produced within the G-quadruplex is expected to experience weak or negligible stabilization by adjacent NDI electron acceptors in the neighboring G-quartet layers. These properties in combination are utilized in the present study to examine the role of the G-quartet/quadruplex core unit in the photoinduced charge-transfer process.

■ EXPERIMENTAL SECTION

Synthesis. The preparation of **1** and its related model compounds is described in detail in the Supporting Information (SI).

Diffusion-Ordered NMR Spectroscopy. The diffusion coefficient (D, related to the hydrodynamic radius, R_h, by the Stokes−Einstein equation) of the G-quadruplex was estimated by diffusion-ordered NMR spectroscopy (DOSY) experiments using a Bruker AVANCE III 600 MHz spectrometer at 298 K in deuterated tetrahydrofuran (THF-d_8). The convection compensated *dstebpgp3s* pulse program,[33,34] with double stimulated echo for convection compensation and longitudinal eddy delay (LED) bipolar gradient pulses for diffusion, was employed. Tetramethylsilane (TMS) is added as the internal reference. The R_h of the G-quadruplex was estimated based on its diffusion coefficient relative to TMS.

Solution Phase X-ray Scattering. Small- and wide-angle X-ray scattering (SAXS/WAXS) measurements were carried out at beamline 12ID-C at the Advanced Photon Source (APS), Argonne National Laboratory. Samples were loaded into 2 mm quartz capillaries with a wall thickness of 0.2 mm. The X-ray scattering instrument utilizes a double-crystal Si(111) monochromator and a two-dimensional mosaic CCD detector. Scattering intensity is reported as a function of the modulus of the scattering vector q, related to the scattering angle 2θ by the equation $q = (4\pi/\lambda) \sin \theta$, where λ is the X-ray wavelength. The sample-to-detector distance was adjusted to measure across two detection ranges of q, 0.006−0.3 Å⁻¹ and 0.1−1.6 Å⁻¹. Subtracting the solvent scattering intensity ($I_{solvent}$) from the sample scattering (I_{sample}) gives the scattering contributed by the solute ($I_{solute} = I_{sample} − I_{solvent}$).

UV−vis Spectroscopy and Electrochemistry. Anhydrous THF was purified on a Glass Contour solvent system. Steady-state absorption spectra were obtained at room temperature on a Shimadzu 1800 UV−vis spectrometer. Electrochemical measurements in THF containing 0.1 M nBu₄NPF₆ electrolyte were performed using a CH Instruments Model 622 electrochemical workstation. A platinum wire counter electrode, Ag/AgCl reference electrode, and a 2 mm diameter platinum or 3 mm glassy carbon disk working electrode were employed. Potentials were calibrated using the ferrocenium/ferrocene (Fc⁺/Fc) couple and referenced to a saturated calomel electrode

(SCE). The electrochemical grade nBu₄NPF₆ was recrystallized twice from hot ethanol prior to use.

Time-Resolved Raman Spectroscopy. Ground-state and time-resolved femtosecond stimulated Raman spectroscopy (FSRS) measurements utilized a 1 kHz Ti:sapphire laser system which has been described previously in detail.[35,36] Briefly, ground-state Raman vibrations are obtained using a 500 nm, spectrally narrow, picosecond Raman pump (SHBC/TOPAS-400, Light Conversion, Inc.) and a femtosecond broadband probe (2 mm sapphire disk) which, together, stimulate the Raman transition. Time-resolved FSRS data are acquired after photochemistry is initiated using a 400 nm femtosecond actinic pump (TOPAS-C, Light Conversion, Inc.). The actinic pump is delayed in time relative to the Raman pump and broadband probe using a mechanical delay stage, and is chopped at 125 Hz. Time-resolved experiments used a 520 nm Raman pump to resonantly enhance GEAn⁺•.

Samples for time-resolved Raman experiments were deoxygenated with argon, sealed in an air free cuvette, and stirred during the full course of the experiment. The concentrations of **GQ-1** samples were identical to those used for NMR and solution phase X-ray scattering (formal concentration of **1** = 3.5 × 10⁻³ M, in the presence of 0.25 equiv KPF₆). The sample of **1** was 7 × 10⁻⁴ M, whereas that of **2** and relevant model compounds were prepared with an o.d. of 1−1.5 at 400 nm.

Kinetic analyses were performed using a linear baseline fitting procedure described previously[35] and at multiple wavelengths using a Levenberg−Marquardt nonlinear least-squares fit to a sum of exponentials convoluted with a Gaussian instrument response function (∼150 fs).

Transient Absorption Spectroscopy. Femtosecond transient absorption (fsTA) measurements at 440−800 nm probe wavelengths were performed using the FSRS setup as described above with no Raman pump. The sample preparation for femtosecond transient absorption is analogous to that used for FSRS experiments.

Samples for nanosecond transient absorption (nsTA) spectroscopy were placed in a 10 mm path length quartz cuvette equipped with a vacuum adapter and subjected to four freeze−pump−thaw degassing cycles. The samples were excited with 7 ns, 1.5 mJ, 416 nm laser pulses generated using the frequency-doubled output of a Continuum Precision II 8000 Nd:YAG laser. The probe light in the nanosecond experiment was generated using a xenon flashlamp (EG&G Electro-optics FX-200) and detected using a photomultiplier tube with high voltage applied to only four dynodes (Hamamatsu R928). The total instrument response function is 7 ns, determined primarily by the laser pulse duration.

Time-Resolved EPR (TREPR) Spectroscopy. TREPR measurements at X-band (9.5 GHz) were performed using a Bruker Elexsys E580 EPR spectrometer outfitted with a variable-Q dielectric resonator (ER-4118X-MD5-W1). Samples were prepared by loading the THF solutions of the monomer **1** and G-quadruplex **GQ-1** into 1.8 mm o.d. (1.5 mm i.d.) quartz tubes, subjecting them to several freeze−pump−thaw degassing cycles, and sealing them using a hydrogen torch. Samples were photoexcited inside the EPR cavity with 416 nm, 1.5 mJ/pulse, 7 ns laser pulses at a 10 Hz repetition rate using the frequency-tripled output of a Spectra Physics Quanta-Ray Pro 350 Nd:YAG laser pumping a Spectra Physics basiScan OPO. The polarization of the laser was set to 54.7° relative to the direction of the static magnetic field to avoid magnetophotoselection effects on the spectra. The field modulation was disabled to achieve a time response of $Q/\pi\nu \approx 30$ ns, where Q is the quality factor of the resonator and ν is the resonant frequency, while microwave signals in emission (e) and/or enhanced absorption (a) were detected in both the real and the imaginary channels (quadrature detection). Sweeping the magnetic field gave 2D spectra versus both time and magnetic field. For each kinetic trace, the signal acquired prior to the laser pulse was subtracted from the data. Kinetic traces recorded at magnetic field values off-resonance were considered background signals, whose average was subtracted from all kinetic traces. The spectra were subsequently phased into a Lorentzian part and a dispersive part, and the former, also known as the imaginary magnetic susceptibility χ'', is presented.
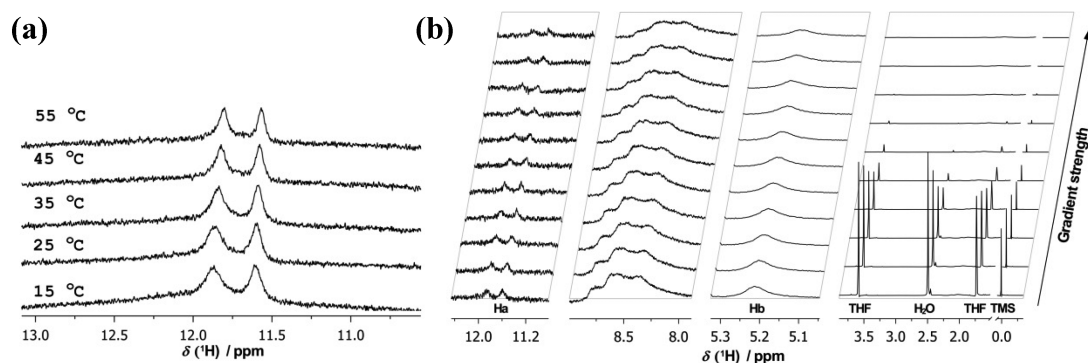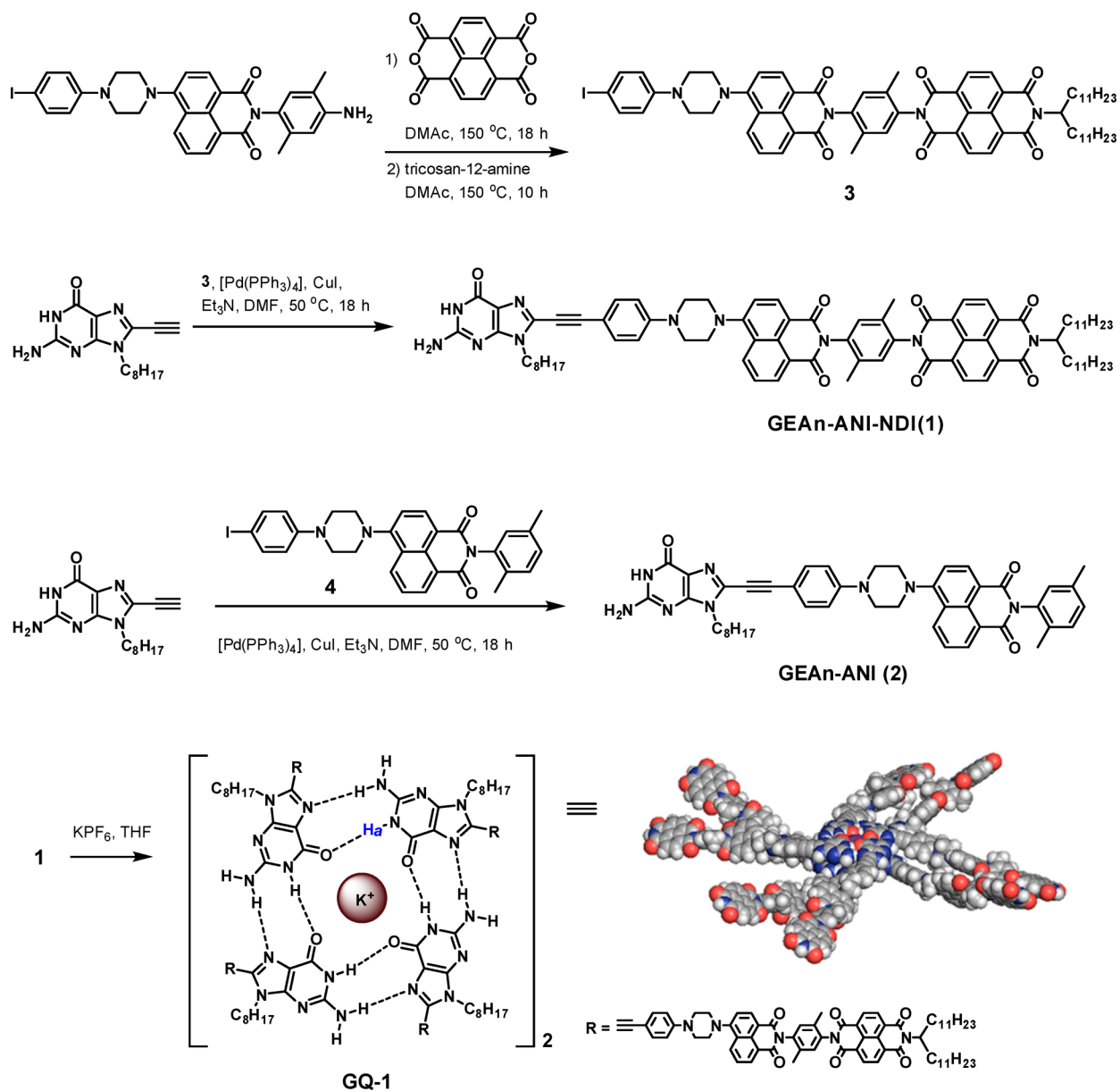
Scheme 1. Synthesis of GEAn-ANI-NDI (1) and GEAn-ANI (2) and Formation of G-Quadruplex

GEAn-ANI-NDI(1)

GEAn-ANI (2)

GQ-1

Figure 1. ^{1}H NMR (600 MHz, THF-d_8) spectra of **GQ-1** (3.5×10^{-3} M of **1** + 0.25 equiv KPF$_6$). (a) Amide region at variable temperatures (15−55 °C). (b) Diffusion-ordered NMR spectroscopy comparing the decay of the signal intensity of **GQ-1**, THF, H$_2$O, and TMS with respect to the gradient strength. H$_a$ = the amido proton, and H$_b$ = the methine proton of the swallowtail. The four ^{1}H NMR regions were scaled differently for easier comparison.
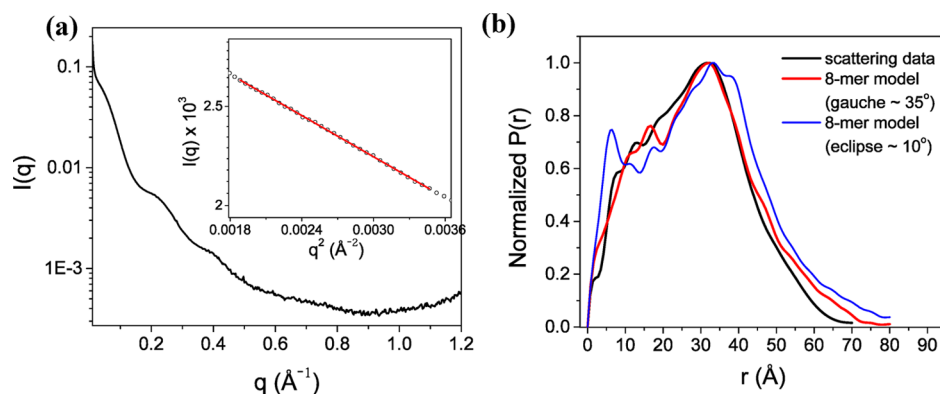
Figure 2. (a) SAXS/WAXS data of **GQ-1** (3.5×10^{-3} M of **1** + 0.25 equiv KPF_6) in THF. Inset shows the Guinier fit of the SAXS data; radius of gyration R_g = 21.5 Å. (b) Comparison of the pair distribution functions (PDFs) generated from the scattering data (black) with that from the structural model (red and blue).

Table 1. Cyclic Voltammetry (CV) and Differential Pulse Voltammetry (DPV) Data in THF[a]

		CV[b]		DPV
	$E°$ (V)	$E_{pa}{}^c$ (V)	ΔE^d (V)	$E_{1/2}$ (V)
1		1.33 ($ANI^{+1/0}$)		1.29
		1.19 ($GEAn^{+2/+1}$)		1.12
		1.00 ($GEAn^{+1/0}$)		0.95
	−0.52 ($NDI^{0/−1}$)		0.11	−0.53
	−1.11 ($NDI^{−1/−2}$)		0.11	−1.12
	−1.30 ($ANI^{0/−1}$)		0.11	−1.31
GQ-1		~1.0^e ($GEAn^{+1/0}$)		~ 0.9 and 1.15^e
	−0.53 ($NDI^{0/−1}$)		0.27	−0.54
	−1.10 ($NDI^{−1/−2}$)		0.26	−1.09
	−1.35 ($ANI^{0/−1}$)		0.24	−1.33

[a]Potentials are given relative to SCE; working electrode = glassy carbon disk (3 mm diameter), counter electrode = Pt wire, reference electrode = Ag/AgCl, supporting electrolyte 0.1 M nBu$_4$NPF$_6$. [b]CV scan rate = 0.1 V s^{-1}. [c]Anodic peak potential. [d]Difference between the anodic and cathodic peak potentials. [e]Unresolved; potentials were estimated.

Simulation of the spectra of the spin-polarized radical pairs[37] was performed using a home-written MATLAB program[38] following published procedures.

RESULTS AND DISCUSSION

Synthesis and G-Quadruplex Formation. Sonogashira coupling between 8-ethynylated guanine and the iodoaniline precursor of **1** gave the guanine-functionalized D−A triad, GEAn-ANI-NDI (**1**) (Scheme 1 and SI). As a model compound for the charge-transfer study, the dyad GEAn-ANI (**2**) was prepared via a similar route. The aryl iodides **3** and **4**, precursors to **1** and **2**, respectively, were prepared by a series of imide condensations and aromatic substitution reactions. A one-pot protocol, consisting of two consecutive condensation reactions, was employed for **3**. The large and flexible tricosan-12-yl aliphatic substituent ("swallowtail") in **1** ensures its solubility and that of its G-quadruplex in THF. In contrast, when an n-dodecyl or 3-pentyl substituent was employed on the terminal NDI nitrogen atom, mixing these soluble guanine triads (**1**-C$_{12}$ and **1**-C$_5$) with KPF$_6$ resulted in cloudy THF solutions, presumably resulting from the formation of large and insoluble oligomeric G-quadruplexes.

Formation of homogeneous and monodisperse G-quadruplexes of **1** (**GQ-1**) was induced by KPF$_6$ in THF ($c = 3.5 \times 10^{-3}$ M at 25 °C, in the presence of 0.25 equiv KPF$_6$), as evidenced by ^{1}H NMR spectroscopy and X-ray scattering experiments. In THF-d_8, the solution of **GQ-1** exhibits two amido resonances at 11.59 and 11.85 ppm, characteristic of C_4 symmetric 8-mer G-quadruplexes (Figure 1);[21,39] the structural integrity persists up to 55 °C. The N^9-methylene protons of the guanine moiety, unfortunately, display an overlapped broad ^{1}H signal, unlike in the case of GPDI-quadruplex in which two distinct sets of ^{1}H signals were observed.[24] Diffusion-ordered NMR spectroscopy (DOSY) experiments (Bruker dstebpgp3s pulse program,[33,34] 600 MHz, 25 °C; SI) reveal that the diffusion coefficient (D) of **GQ-1** is 10 ± 1 times smaller than D_{TMS} (TMS = tetramethylsilane, Figure 1b), consistent with the existence of a supramolecular entity.

The structure of **GQ-1** was further evaluated by SAXS/WAXS experiments. Figure 2a shows a plot of the logarithm of the scattering intensity $[I(q)]$ versus the modulus of the scattering vector (q). Guinier analysis[40] at the low q region (0.043−0.059 Å^{-1}) gives the radius of gyration R_g = 21.5 Å. The atomic pair−distance distribution functions (PDF) based on the experimental $I(q)$ at q = 0−1.2 Å^{-1} and on the structural models of C_4 symmetric **GQ-1** optimized[41] with the MMFF94s force field were constructed by GNOM[42] and overlaid in Figure 2b for comparison. From the experimental scattering data, the PDF shows significant probability density (normalized $P(r)$ > 0.5) in the region of 6−44 Å with the highest probability at 32 Å. These features were well reproduced by the simulated PDF of the C_4 8-mer model (Scheme 1), supporting the structural

assignments based on ^{1}H NMR. The radius $R \sim 35$ Å of **GQ-1**, approximated by the length of the aromatic unit in **1**, is comparable to the distance at which the maximum $P(r)$ was found in the PDFs. Furthermore, estimation of the radius of gyration for a columnar object by $R^2_{g,calc.} = R^2/2 + h^2/12$, where R is the radius and h the height (3.5 Å) of the column, suggests $R_{g,calc.} = 24.8$ Å, similar to $R_g = 21.5$ Å found by SAXS.

It is important to note that there is only minor overlap between the ANI-NDI subunits in **GQ-1**. A relative rotation angle of ca. 35° about the C_4 axis between each layer is necessary to produce a good fit to the experimental PDF; a much poorer match was observed based on the structural models with a ca. 10° rotation (blue curve in Figure 2b), an angle found in the case of the GPDI-quadruplex reported earlier.[24] In the latter case, the strong π−π interactions between the peripheral PDI units place the chromophores in register.

Electrochemistry of the Monomeric Triad and G-Quadruplex. The energetics of the photogenerated RPs relative to the ground and excited states can be estimated from the one-electron redox potentials for the donors and acceptors (0.1 M nBu$_4$PF$_6$ in THF; redox potentials in Table 1 are reported relative to SCE). For the monomers, the reduction potentials measured for ANI ($E_{red} = -1.31$ (**1**) or -1.35 (**2**) V vs SCE) and NDI ($E_{red1} = -0.53$ and E_{red2} -1.12 V) moieties are similar to the reported values.[30,31] The GEAn donor exhibits two irreversible oxidation waves about $E_{ox1} = +0.95$ and $E_{ox2} = +1.12$ V. Additionally, the one-electron oxidation of ANI is observed at $E_{ox} = +1.29$ V. Based on these values, GEAn$^{+\bullet}$-ANI$^{-\bullet}$-NDI and GEAn$^{+\bullet}$-ANI-NDI$^{-\bullet}$ are 2.3 and 1.6 eV, respectively, above the ground state and are expected to form sequentially after photoexcitation of ANI ($E_S(^1$*ANI) = 2.80 eV, see SI).

The redox potentials of self-assembled **GQ-1** remain largely similar to those of monomeric **1**, with the exception that the irreversible oxidation waves are less well resolved for **GQ-1**. Nevertheless, the onset potentials of the first oxidation waves for **1** or **GQ-1** are both around +0.92 V. On the reduction side, two sets of overlapping reduction waves with equal currents were observed for E_{red1}(NDI), E_{red2}(NDI), and E_{red}(ANI). The average potentials of the two overlapping E_{red}(ANI) and E_{red1}(NDI) waves for **GQ-1** (-1.33 and -0.54 V, respectively) are virtually identical to those for monomeric **1** (-1.31 and -0.53 V, respectively), suggesting that the photoinduced ion pairs (GEAn$^{+\bullet}$-ANI$^{-\bullet}$-NDI and GEAn$^{+\bullet}$-ANI-NDI$^{-\bullet}$) have similar energies in **GQ-1** and **1**.

Photoinduced Charge Separation. Time-resolved transient absorption studies elucidate the dynamics of photoinduced charge separation in **1**, **GQ-1**, and model compound **2**. Based on the ion-pair energetics, we expect **1** and **GQ-1** to undergo two-step charge transfer: GEAn-^{1}*ANI-NDI → GEAn$^{+\bullet}$-ANI$^{-\bullet}$-NDI → GEAn$^{+\bullet}$-AN-NDI$^{-\bullet}$. Evaluation of **2** as a model D−A dyad provides insights into the first charge separation step (Figure 3). Indeed, excitation of ANI in molecule **2** at 400 nm populates ^{1}*ANI, indicated by the positive absorption band at 447 nm and simulated emission at 490 nm.[30] The decay of this state is accompanied by a rise (τ_{CS} = 5 ps) of the ANI$^{-\bullet}$ band at 450 nm and a second feature at 510 nm. Both peaks decay with τ_{CR} = 680 ps. The coincident rise of the 510 nm absorption band with the ANI$^{-\bullet}$ feature suggests that it results from GEAn$^{+\bullet}$. The nature of this band will be discussed in more detail below.

Similar charge-transfer behavior occurs in compound **1** at early times: population of ^{1}*ANI is followed by the formation
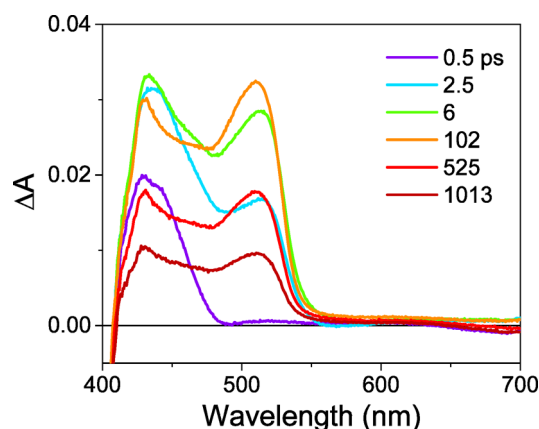

Figure 3. Femtosecond transient absorption spectra for **2** in THF.

of ANI$^{-\bullet}$ in τ_{CS1} = 5 ps. However, in contrast to charge recombination in **2**, a charge shift from ANI$^{-\bullet}$ to NDI occurs in τ_{CS2} = 330 ps, indicated by the appearance of the NDI$^{-\bullet}$ absorption at 480 and 605 nm (Figure 4a, time constants obtained from the average of the single-wavelength fit at 470 and 517 nm).[30] The growth of the NDI$^{-\bullet}$ bands is accompanied by a sharpening of the broad 510 nm peak. The quantum yield of the charge shift reaction is 66% based on the relative time constants of the charge shift reaction for **1** (330 ps) and the charge recombination for **2** (680 ps). Nanosecond transient absorption experiments reveal that GEAn$^{+\bullet}$-ANI-NDI$^{-\bullet}$ exhibits a biexponential decay to ground state with a major ~300 ns component and a minor ~1 μs component (Figure 4b), which will be discussed in detail below.

Excitation of **GQ-1** at 400 nm also generates long-lived GEAn$^{+\bullet}$-ANI-NDI$^{-\bullet}$, where the two charge-transfer steps occur in τ_{CS1} = 10 ps and τ_{CS2} = 110 ps. In contrast to **1**, no sharpening of the 510 nm band occurs in concert with the charge shift reaction. The small changes in the charge separation time constants for the two-step formation of GEAn$^{+\bullet}$-ANI-NDI$^{-\bullet}$ in **GQ-1** relative to **1** are most likely attributable to small changes in ΔG for these charge separation reactions either because of small, unresolved GEAn oxidation potential changes by being incorporated into the quadruplex and/or by exclusion of solvent from one face of the quadruplex structure resulting in small changes in the solvent reorganization energies for the electron-transfer reactions.[43,44] Recently, it was reported that the proton dissociation rate in small G-quadruplexes in water is ~2 × 10^5 s^{-1}, which is substantially slowed relative to G$^{+\bullet}$,[45] so that it is unlikely that proton loss competes with charge recombination in **1** and **GQ-1** in lower polarity THF as measured here. The NDI$^{-\bullet}$ absorption at 470 nm in **GQ-1** again exhibits a biexponential decay in which the two components are ~300 ns and ~1 μs; however, unlike **1**, the amplitudes of the two components in **GQ-1** are similar (Figure 5b), which will be discussed in detail below.

Extension of the charge separation lifetime upon G-quadruplex assembly has been observed previously in the self-assembly of G-PDI.[24] In the present case, the charge separation lifetime of GEAn$^{+\bullet}$-ANI-NDI$^{-\bullet}$ increases only 5-fold upon G-quadruplex formation. The smaller increase in lifetime compared to the G-PDI quadruplex is likely due to less stabilization of NDI$^{-\bullet}$ in **GQ-1** relative to PDI$^{-\bullet}$ in the PDI system, wherein the photogenerated PDI$^{-\bullet}$ is stabilized by charge sharing between the stacked PDIs. As discussed above,
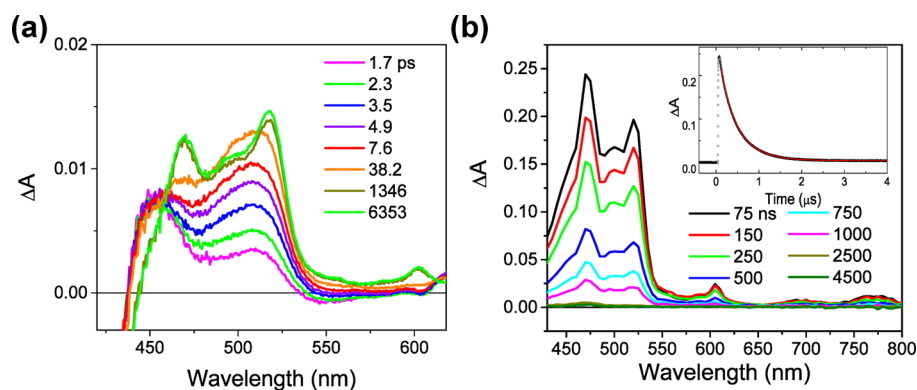
Figure 4. Femtosecond (a) and nanosecond (b) transient absorption spectra and kinetics at 470 nm (inset) for **1** in THF.
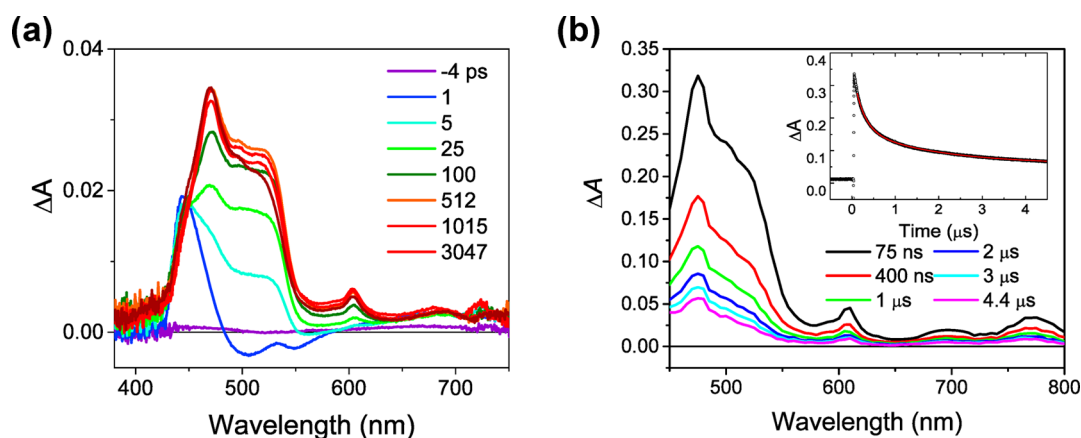

Figure 5. Femtosecond (a) and nanosecond (b) transient absorption spectra and kinetics at 470 nm (inset) for **GQ-1** in THF.

the spatial and orbital overlap between NDIs is minimal, compromising any stabilization effects.

The assignment of the 510 nm band to GEAn$^{+\bullet}$ is supported by time-dependent density functional theory (TD-DFT) calculations at the ωB97X-D/6-311G** or B3LYP/6-311G** level of theory in THF (CPCM solvation) on the gas-phase optimized structure (B3LYP/6-31G*). Direct measurement of the GEAn$^{+\bullet}$ absorption by spectroelectrochemistry is complicated by the electrochemical instability of this radical cation. The 510 nm GEAn$^{+\bullet}$ band correlates with several computed high-energy transitions ($D_{3-5} \leftarrow D_0$) of GEAn$^{+\bullet}$ centered around 452 nm. Additionally, the lowest-energy transition ($D_1 \leftarrow D_0$) computed at 1080 nm was observed at 1100 nm using near-infrared transient absorption spectroscopy (Figure S3). The reliability of this DFT-based assignment was tested on two model compounds, **BuEAnANI** and **PhEAnANI**, which replace the guanine moiety of **2** with a butyl or phenyl group, respectively. The computed $D_1 \leftarrow D_0$ transitions of BuEAn$^{+\bullet}$ at 545 nm and PhEAn$^{+\bullet}$ at 660 nm are corroborated by the observed transient absorption bands at 593 nm for BuEAn$^{+\bullet}$ in **BuEAnANI** and 700 nm for PhEAn$^{+\bullet}$ in **PhEAnANI** (λ_{exc} = 400 nm, Figure S4).

Hole Transfer Dynamics. The transient absorption data provide initial insights into the differences in the electronic/structural nature of GEAn$^{+\bullet}$ in the monomeric and self-assembled states. The sharpening of the GEAn$^{+\bullet}$ absorption in **1** as the charge shifts from ANI$^{-\bullet}$ to NDI suggests that the hole experiences a different electronic environment in the monomer relative to that in the G-quadruplex. To further investigate this effect, we employed FSRS, which provides a more direct

method to probe the structural effects of charge separation.[35] Both the ground- and excited-state Raman spectra of **1** and **GQ-1** are described below and compared with the model compounds.

Ground-State Raman Spectra. The ground-state Raman spectrum of **1** is shown in Figure 6 (black trace) and displays vibrations from GEAn (green trace), ANI (blue trace), and NDI (red trace) individual components. The peak assignments for each subunit and molecule **1** are summarized in Table 2.

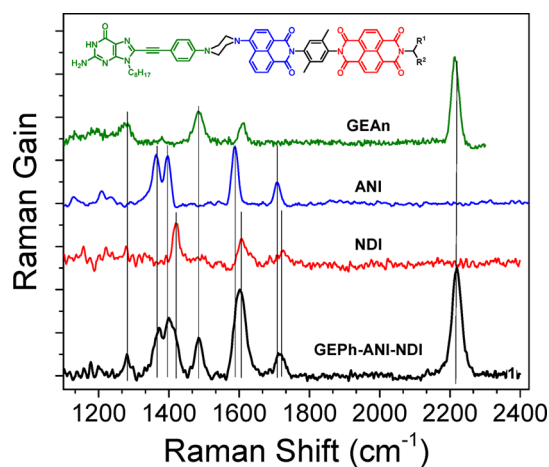**Figure 6.** Ground-state Raman spectra of **1** (black), NDI (red), GEAn (green), and ANI (blue). All spectra were acquired in THF with a 500 nm Raman pump (1 μJ/pulse).

Table 2. Ground-State Raman Peak Assignments

compound **1** (cm^{-1})	components in compound **1** (cm^{-1})		
	GEAn	ANI	NDI
2219	2208		
1709	1711	1709	1725
1602	1597	1590	1605
1486	1482		
1420			1418
1396		1396	
1364		1364	
1279	1274		

DFT calculations (SI) at the B3LYP/6-31G* level of theory indicate that the C=O stretches of NDI and ANI comprise the 1709 cm^{-1} vibration, while the 1602, 1420, and 1396 cm^{-1} modes are the in-plane C=C stretches of NDI and ANI. The most distinct GEAn vibrational modes are observed at 1274, 1482, 1597, and 2208 cm^{-1}. For GEAn, the high-frequency 2208 cm^{-1} vibration is the symmetric C≡C stretch, the vibrations between 1200 and 1500 cm^{-1} are both in-plane guanine C=C/C=N and phenyl C=C vibrations, and the band at 1597 cm^{-1} consists solely of the C=C stretches from the phenyl moiety.

The ground-state Raman spectra of **1** and **GQ-1** are very similar. This is somewhat surprising because hypsochromic frequency shifts (~5 cm^{-1}) upon hydrogen bonding and quadruplex assembly have previously been observed and computed for guanosine-based assembled systems.[46] The presence of the phenyleneethynylene group on the 8-position of guanine results in delocalization of the vibrational modes over these strongly coupled moieties, and thus further diminishes the already small frequency shifts expected from quadruplex assembly to form **GQ-1**. Additionally, strong overlap with the THF solvent modes occurs, making small changes difficult to observe, even after background subtraction (Figure S5).

Time-Resolved Raman Spectra. Figure 7 shows time-resolved FSRS spectra of **1**, **2**, and **GQ-1** alongside their respective ground-state spectra. The Raman pump wavelength (λ_{RP} = 520 nm) was chosen to enhance the vibrations coupled to the GEAn$^{+\bullet}$ electronic transition. The transient spectra reveal peaks at 1195, 1240, 1376, 1481, and 2126 cm^{-1} for **1** and **GQ-1**. The peak intensities for **1** rise biexponentially with time constants similar to τ_{CS1} and τ_{CS2} observed in the transient absorption spectra and persist for the duration of the

experiment (7 ns). The persistent nature of these vibrations is consistent with a long-lived, charge-separated state. The same modes observed in **GQ-1** appear biexponentially, matching τ_{CS1} and τ_{CS2}. Similarly, photoexcitation of **2** at 400 nm reveals vibrations at 1197, 1243, 1479, 1590, and 2122 cm^{-1}, whose mode intensities rise and decay with time constants consistent with charge separation and charge recombination.

We attribute the peaks at 1197, 1243, 1479, and 2122 cm^{-1} to GEAn$^{+\bullet}$. This is supported by the retention of the vibrational modes through the two charge separation steps. The rise or decay of any mode with the kinetics of the charge shift would assign those modes to NDI or ANI, respectively. Unfortunately, explicit assignment of the GEAn excited-state vibrational modes is complicated by the delocalized nature of guanine vibrations and anharmonic and vibrational coupling between modes.[47] While one- and two-dimensional infrared spectroscopies have been used to probe these effects in both the ground and excited states, no studies have employed time-resolved Raman spectroscopy on the charge-transfer dynamics of nucleobases. However, based on the DFT computations, we can confidently assign the ~2120 cm^{-1} mode to the ethynyl stretch in GEAn$^{+\bullet}$, and this will be the primary mode considered. Any further explicit assignment of the observed vibrations is beyond the scope of this study.

In contrast to the aforementioned peaks, the 1590 cm^{-1} mode is only observed in **1** and **2**, and the 1427 cm^{-1} mode only in **1** and **GQ-1**. We assign the 1427 cm^{-1} vibration to NDI$^{-\bullet}$ as it closely matches that acquired by resonance Raman characterization of chemically reduced NDI (Figure S7). The absence of the 1590 cm^{-1} mode in **GQ-1** is more difficult to rationalize. This vibration is close in proximity to the C=O and C=C stretches of NDI and ANI, and we cannot find any physical reason for its absence in the spectra of **GQ-1**. Instead, we tentatively attribute this to the strong overlap of the ground-state spectrum of **GQ-1** with its RP spectrum. The increased concentration of **GQ-1** compared to **1** and **2** induces overlap of ground-state modes with the RP modes (SI). In some cases, modes of weaker intensity may be obscured by incompletely subtracted ground-state vibrations if the vibrational shift or Raman intensity does not substantially differ in the photo-initiated states.

Most importantly, we observe a time-dependent frequency shift of the ethynyl vibration in compound **1** which is not apparent in **GQ-1** (Figure 8). This frequency shift is unique to the ethynyl mode and is not observed in any lower frequency vibrations. Upon photoexcitation, the ethynyl band in **1** and
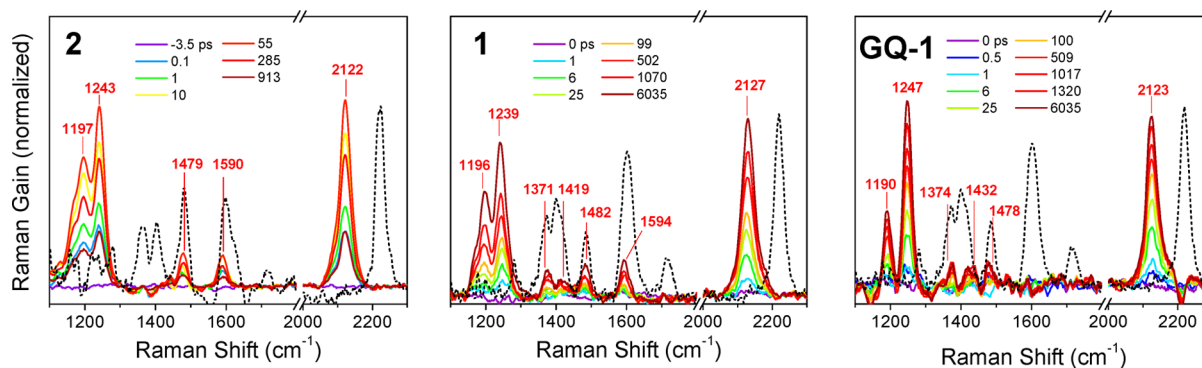

Figure 7. Ground-state (dotted black line) and time-resolved excited-state Raman spectra of **2**, **1**, and **GQ-1**. All spectra are acquired in THF with a 520 nm Raman pump following 400 nm photoexcitation.
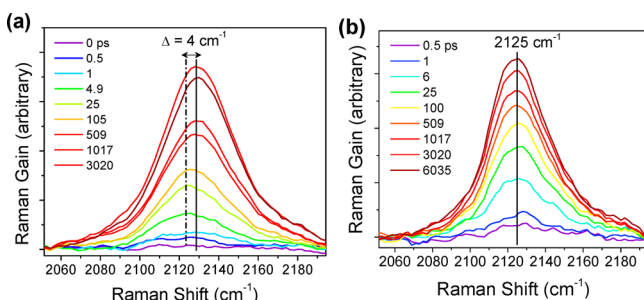
Figure 8. Time-resolved Raman spectra of the ethynyl vibration in (a) **1** and (b) **GQ-1**.

GQ-1 appears at 2125 cm^{-1}. In **1**, this mode shifts from 2125 to 2129 cm^{-1} over the time scale of the charge shift ($\tau_{CS2} = 330$ ps). This slight increase in frequency is indicative of an increased force constant of the ethynyl stretch as the electron moves from ANI$^{-\bullet}$ to NDI. Additionally, the time scale of the peak shift tracks with the narrowing of the 510 nm absorption band in the femtosecond transient absorption spectra.

In the case of **GQ-1**, the position of the 2125 cm^{-1} band remains constant with time. This observation suggests there is little change in the overall electronic structure of the G-quadruplex upon hole injection and charge shifting. This matches the findings from transient absorption experiments, where the transient signal of GEAn$^{+\bullet}$ remained unchanged over the charge separation process. The lack of significant structural changes implied by the unchanged vibrational frequency suggests either that GEAn$^{+\bullet}$ does not delocalize in the same G-quartet plane via H-bonding or between G-quartet layers via $\pi-\pi$ interactions or that a delocalized cation forms faster than about 1 ps upon excitation. The latter argument is supported by the retention of the broadened 510 nm transient absorption signal as the charge shift occurs.

Spin Dynamics and Radical Ion Pair Recombination. Photoexcitation of the ANI chromophore in **1** to its excited singlet state results in formation of the singlet RP, ^{1}(GEAn$^{+\bullet}$-ANI-NDI$^{-\bullet}$), which may undergo radical pair intersystem crossing (RP-ISC) driven largely by electron−nuclear hyperfine couplings in a few nanoseconds to produce the triplet RP, ^{3}(GEAn$^{+\bullet}$-ANI-NDI$^{-\bullet}$).[48,49] The long distance between the two radicals results in a small zero-field splitting of the triplet RP sublevels resulting from the dipolar interaction (d) between the two spins, which is largely averaged out in solution. The energy gap between the nearly degenerate three triplet RP sublevels and the singlet RP is determined by the spin−spin exchange interaction ($2J$, Figure 9a). The subsequent RP
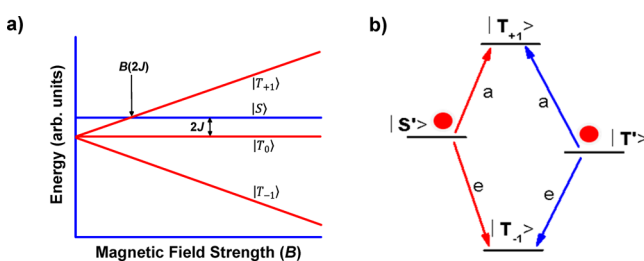
recombination process is spin selective in that the singlet RP recombines to the singlet ground state, whereas the triplet RP recombines to a locally excited neutral triplet state, if this state is lower in energy than the triplet RP.[50] For GEAn-ANI-NDI, the lowest excited triplet state resides on NDI and has an energy of 2.03 eV;[51] thus the 1.6 eV energies of the triplet sublevels of ^{3}(GEAn$^{+\bullet}$-ANI-NDI$^{-\bullet}$) are about 0.7 eV below ^{3*}NDI; thus precluding charge recombination via the triplet channel. Under these conditions, RP-ISC may still may occur to populate all three triplet sublevels of ^{3}(GEAn$^{+\bullet}$-ANI-NDI$^{-\bullet}$), provided that $2J$ is small.

TREPR spectroscopy using pulsed laser excitation and continuous microwaves was employed to obtain J for the photogenerated RPs in **1** and **GQ-1**. At the ∼340 mT magnetic field characteristic of EPR measurements at X-band, the three RP triplet states are Zeeman split resulting in the four-state energy level diagram illustrated in Figure 9b in which RP-ISC results in S−T$_0$ mixing to produce the coherent superposition states |S′⟩ and |T′⟩.[52] Microwave-induced transitions between these states and the |T$_{+1}$⟩ and |T$_{-1}$⟩ states result in a spin-polarized EPR spectrum with four lines having a symmetric (e,a,e,a) antiphase pattern (where e denotes emission and a denotes enhanced absorption, low to high field), provided that the spin−spin exchange interaction (J) is positive and larger than the spin−spin dipolar interaction (d). If the g-factors of the two radicals are similar and/or the transitions are split by hyperfine coupling, the two doublets will overlap significantly and will appear as a distorted (e,a) signal.[48,49] The spin polarization pattern (whether a transition is e or a) is also determined by the sign rule, $\Gamma = \mu \cdot \text{sign}[2J - d(3\cos^2\theta - 1)]$, where $\mu = -1$ or $+1$ if the spin-correlated radical pair (SCRP) is produced from a singlet or triplet precursor, respectively, and θ is the angle between the vector connecting the two spins and the externally applied magnetic field.[52] For $\Gamma = (-)$ the observed phase is (e,a), whereas for $\Gamma = (+)$ the phase is (a,e). As noted above, in isotropic solutions, d is rotationally averaged to zero, and RP-ISC depends on the magnitude of J which depends exponentially on the distance, r, between the individual radicals comprising the radical pair.

The results from measurements carried out at X-band (9.5 GHz) in THF at 298 K are shown in Figure 10 at the times indicated. The spectra were simulated with the SCRP model[37] using previously reported values for the hyperfine coupling constants (HFCCs) for NDI$^{-\bullet}$.[32] Due to the chemical instability of GEAn$^{+\bullet}$, HFCCs and the isotropic g-factor for GEAn$^{+\bullet}$ were calculated using DFT. Computational details and the fitting parameters for the simulations that yield J are listed in Table S4. Monomeric **1** in THF gives a RP signal ($J = 5.5$ μT) in which hyperfine structure appears and decays with time. The exchange interaction is significantly reduced with respect to similar electron D−A systems bearing other donors due to the weaker electronic coupling between GEAn$^{+\bullet}$ and NDI$^{-\bullet}$ resulting from the longer distance between their average spin distributions.[32,53] Simulations of the **GQ-1** data yield a similar, yet smaller exchange interaction ($J = 4.5$ μT). The differences in the time evolution of the TREPR spectra between **1** and **GQ-1** most likely result from differing spin−lattice relaxation times of the RPs. Given that J depends exponentially on distance, the fact that J for GEAn$^{+\bullet}$-ANI-NDI$^{-\bullet}$ in **1** is somewhat larger than in **GQ-1** results suggest that the average distance between the spin density distributions of the two radicals within the RP are somewhat larger in **GQ-1** relative to **1**.

Figure 9. (a) Zeeman splitting of RP energy levels ($J > 0$). (b) Relative energies of the RP spin states. The initial spin populations following S−T$_0$ mixing are indicated by the solid red dots. The arrows indicate the microwave-induced transitions responsible for the observed spin-polarized TREPR spectrum.
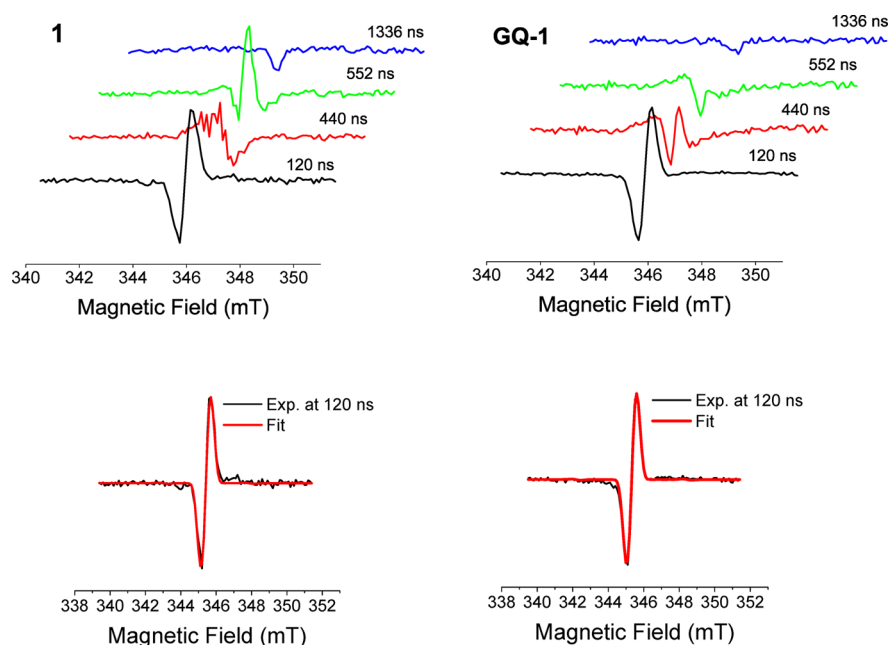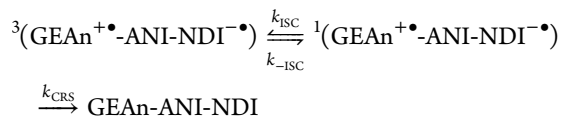
Figure 10. TCW-EPR spectra of **1** (top left) and **GQ-1** (top right) at X-band in THF at 298 K. Bottom: Simulations of the 120 ns time slices of **1** (bottom left) and **GQ-1** (bottom right).

Since the TREPR spectra show that the J values for the RPs in both **1** and **GQ-1** are very small, RP-ISC at zero magnetic field readily occurs to populate the three triplet sublevels of ^{3}(GEAn$^{+\bullet}$-ANI-NDI$^{-\bullet}$), whose populations rapidly equilibrate via spin relaxation. Subsequent reverse RP-ISC back to ^{1}(GEAn$^{+\bullet}$-ANI-NDI$^{-\bullet}$) must necessarily precede charge recombination to the singlet ground state. Under these conditions, a simple equilibrium model:

$$^3(\text{GEAn}^{+\bullet}\text{-ANI-NDI}^{-\bullet}) \underset{k_{-\text{ISC}}}{\overset{k_{\text{ISC}}}{\rightleftharpoons}} {}^1(\text{GEAn}^{+\bullet}\text{-ANI-NDI}^{-\bullet})$$

$$\overset{k_{\text{CRS}}}{\longrightarrow} \text{GEAn-ANI-NDI}$$

can be used to model the charge recombination.[54,55] Monitoring the total population of NDI$^{-\bullet}$, the nsTA kinetic data were fit at 470 nm using this model (insets to Figures 4b and 5b). For monomer **1** this results in $k_{\text{CRS}} = (3.0 \pm 0.1) \times 10^6$ s^{-1}, $k_{\text{ISC}} = (4.7 \pm 0.1) \times 10^5$ s^{-1}, and $k_{-\text{ISC}} = (3.4 \pm 0.1) \times 10^6$ s^{-1}, while the corresponding values for **GQ-1** are $k_{\text{CRS}} = (2.9 \pm 0.1) \times 10^6$ s^{-1}, $k_{\text{ISC}} = (1.1 \pm 0.1) \times 10^6$ s^{-1}, and $k_{-\text{ISC}} = (8.1 \pm 0.1) \times 10^5$ s^{-1}. Note that the intrinsic charge recombination rate from the singlet RP to ground state is the same for both **1** and **GQ-1**, while the equilibrium RP population is shifted toward the triplet radical pair in **GQ-1** relative to **1**, resulting in an increase in the amplitude of the microsecond decay component in **GQ-1**. The comparable charge-recombination rates, k_{CRS}, are consistent with the similar ΔG_{CR} for both **1** and **GQ-1**. The additional hyperfine couplings resulting from the interaction of GEAn$^{+\bullet}$ with its hydrogen-bonded neighbors in **GQ-1** relative to their absence in **1** suggest that spin (charge) delocalization onto the additional guanines occurs. RP-ISC theory shows that the ISC rate depends on the nuclear spin-state weighted sum of the hyperfine couplings within the radicals,[52] so that the larger number of hyperfine interactions **GQ-1** relative to monomer **1** results in more rapid RP-ISC in **GQ-1**.

CONCLUSION

A K$^+$-induced G-quadruplex is exploited as a supramolecular platform to organize GEAn-ANI-NDI triad **1** into a concentric D−A architecture, in which minimal intraquadruplex spatial overlap between the electron-accepting ANI-NDI units was revealed by the SAXS/WAXS experiments. The results of the fsTA, nsTA, FSRS, and TREPR measurements combine to present a picture of how the G-quadruplex structure influences hole movement in **GQ-1**. Compared with monomeric **1**, overall photoinduced charge separation in **GQ-1** to produce GEAn$^{+\bullet}$-ANI-NDI$^{-\bullet}$ is about three times faster and is not accompanied by significant structural changes. Charge recombination depends on GEAn$^{+\bullet}$-ANI-NDI$^{-\bullet}$ spin dynamics with a significant ~1 μs lifetime component within **GQ-1** produced by enhanced RP-ISC attributed to a greater number of hyperfine couplings in the assembly. Consistent with this picture, TREPR spectroscopy indicates that the positive charge of photogenerated GEAn$^{+\bullet}$ is slightly more dispersed in **GQ-1** relative to **1**, even though FSRS suggests that GEAn$^{+\bullet}$ in the G-quadruplex experiences negligible structural reorganization during its ultrafast formation. This indicates that hole sharing between the guanines in the G-quadruplex core of **GQ-1** may occur concurrently with photodriven hole injection into the core. The ability of G-quadruplex structures to rapidly transport holes makes this self-assembly motif particularly appealing for the design of novel D−A molecules having segregated charge conduits in which the oxidized donors and reduced acceptors transport charge long distances.

ASSOCIATED CONTENT

Ⓢ Supporting Information

Experimental details including synthesis, DOSY, SAXS/WAXS, transient absorption, supplementary Raman spectra, EPR parameters, and DFT computational results. This material is available free of charge via the Internet at http://pubs.acs.org.

■ AUTHOR INFORMATION

Corresponding Authors
*yi-lin.wu@northwestern.edu
*m-wasielewski@northwestern.edu

Notes
The authors declare no competing financial interest.

■ REFERENCES

(1) Wasielewski, M. R. *J. Org. Chem.* **2006**, *71*, 5051.

(2) Wasielewski, M. R. *Acc. Chem. Res.* **2009**, *42*, 1910.

(3) Kargul, J.; Nield, J.; Barber, J. *J. Biol. Chem.* **2003**, *278*, 16135.

(4) Umena, Y.; Kawakami, K.; Shen, J. R.; Kamiya, N. *Nature* **2011**, *473*, 55.

(5) McDermott, G.; Prince, S. M.; Freer, A. A.; Hawthornthwaite-Lawless, A. M.; Papiz, M. Z.; Cogdell, R. J.; Isaacs, N. W. *Nature* **1995**, *374*, 517.

(6) Würthner, F. *Chem. Commun.* **2004**, 1564.

(7) Rieth, S.; Li, Z.; Hinkle, C. E.; Guzman, C. X.; Lee, J. J.; Nehme, S. I.; Braunschweig, A. B. *J. Phys. Chem. C* **2013**, *117*, 11347.

(8) van der Boom, T.; Hayes, R. T.; Zhao, Y.; Bushard, P. J.; Weiss, E. A.; Wasielewski, M. R. *J. Am. Chem. Soc.* **2002**, *124*, 9582.

(9) Sinks, L. E.; Rybtchinski, B.; Iimura, M.; Jones, B. A.; Goshe, A. J.; Zuo, X.; Tiede, D. M.; Li, X.; Wasielewski, M. R. *Chem. Mater.* **2005**, *17*, 6295.

(10) Lefler, K. M.; Co, D. T.; Wasielewski, M. R. *J. Phys. Chem. Lett.* **2012**, *3*, 3798.

(11) Rybtchinski, B.; Sinks, L. E.; Wasielewski, M. R. *J. Am. Chem. Soc.* **2004**, *126*, 12268.

(12) Roznyatovskiy, V. V.; Carmieli, R.; Dyar, S. M.; Brown, K. E.; Wasielewski, M. R. *Angew. Chem., Int. Ed.* **2014**, *53*, 3457.

(13) Bullock, J. E.; Carmieli, R.; Mickley, S. M.; Vura-Weis, J.; Wasielewski, M. R. *J. Am. Chem. Soc.* **2009**, *131*, 11919.

(14) Yamamoto, Y.; Fukushima, T.; Suna, Y.; Ishii, N.; Saeki, A.; Seki, S.; Tagawa, S.; Taniguchi, M.; Kawai, T.; Aida, T. *Science* **2006**, *314*, 1761.

(15) Saeki, A.; Koizumi, Y.; Aida, T.; Seki, S. *Acc. Chem. Res.* **2012**, *45*, 1193.

(16) Sforazzini, G.; Turdean, R.; Sakai, N.; Matile, S. *Chem. Sci.* **2013**, *4*, 1847.

(17) Jin, S.; Ding, X.; Feng, X.; Supur, M.; Furukawa, K.; Takahashi, S.; Addicoat, M.; El-Khouly, M. E.; Nakamura, T.; Irle, S.; Fukuzumi, S.; Nagai, A.; Jiang, D. *Angew. Chem., Int. Ed.* **2013**, *52*, 2017.

(18) Chen, L.; Furukawa, K.; Gao, J.; Nagai, A.; Nakamura, T.; Dong, Y.; Jiang, D. *J. Am. Chem. Soc.* **2014**, *136*, 9806.

(19) Wilson, A.; Gasparini, G.; Matile, S. *Chem. Soc. Rev.* **2014**, *43*, 1948.

(20) Hartnett, P. E.; Dyar, S. M.; Margulies, E. A.; Shoer, L. E.; Cook, A. W.; Eaton, S. W.; Marks, T. J.; Wasielewski, M. R. *Chem. Sci.* **2014**, *6*, 402.

(21) González-Rodríguez, D.; van Dongen, J. L. J.; Lutz, M.; Spek, A. L.; Schenning, A. P. H. J.; Meijer, E. W. *Nat. Chem.* **2009**, *1*, 151.

(22) Lena, S.; Masiero, S.; Pieraccini, S.; Spada, G. P. *Chem.—Eur. J.* **2009**, *15*, 7792.

(23) Davis, J. T.; Spada, G. P. *Chem. Soc. Rev.* **2007**, *36*, 296.

(24) Wu, Y.-L.; Brown, K. E.; Wasielewski, M. R. *J. Am. Chem. Soc.* **2013**, *135*, 13322.

(25) Graziano, C.; Masiero, S.; Pieraccini, S.; Lucarini, M.; Spada, G. P. *Org. Lett.* **2008**, *10*, 1739.

(26) Forman, S. L.; Fettinger, J. C.; Pieraccini, S.; Gottareli, G.; Davis, J. T. *J. Am. Chem. Soc.* **2000**, *122*, 4060.

(27) Delaney, S.; Barton, J. K. *Biochemistry* **2003**, *42*, 14159.

(28) Cauët, E. *J. Biomol. Struct. Dyn.* **2011**, *29*, 557.

(29) Choi, J.; Park, J.; Tanaka, A.; Park, M. J.; Jang, Y. J.; Fujitsuka, M.; Kim, S. K.; Majima, T. *Angew. Chem., Int. Ed.* **2012**, *52*, 1134.

(30) Greenfield, S. R.; Svec, W. A.; Gosztola, D.; Wasielewski, M. R. *J. Am. Chem. Soc.* **1996**, *118*, 6767.

(31) Miller, S. E.; Lukas, A. S.; Marsh, E.; Bushard, P.; Wasielewski, M. R. *J. Am. Chem. Soc.* **2000**, *122*, 7802.

(32) Colvin, M. T.; Carmieli, R.; Miura, T.; Richert, S.; Gardner, D. M.; Smeigh, A. L.; Dyar, S. M.; Conron, S. M.; Ratner, M. A.; Wasielewski, M. R. *J. Phys. Chem. A* **2013**, *117*, 5314.

(33) Jerschow, A.; Müller, N. *J. Magn. Reson.* **1997**, *125*, 372.

(34) Jerschow, A.; Müller, N. *J. Magn. Reson.* **1998**, *132*, 13.

(35) Brown, K. E.; Veldkamp, B. S.; Co, D. T.; Wasielewski, M. R. *J. Phys. Chem. Lett.* **2012**, *3*, 2362.

(36) Young, R. M.; Dyar, S. M.; Barnes, J. C.; Juricek, M.; Stoddart, J. F.; Co, D. T.; Wasielewski, M. R. *J. Phys. Chem. A* **2013**, *117*, 12438.

(37) Till, U.; Hore, P. J. *Mol. Phys.* **1997**, *90*, 289.

(38) *MATLAB*; The MathWorks, Inc.: Natick, MA, 2013.

(39) Masiero, S.; Trotta, R.; Pieraccini, S.; De Tito, S.; Perone, R.; Randazzo, A.; Spada, G. P. *Org. Biomol. Chem.* **2010**, *8*, 2683.

(40) Guinier, A.; Fournet, G. *Small-Angle Scattering of X-rays*; John Wiley & Sons, Inc.: New York, 1955.

(41) Hanwell, M. D.; Curtis, D. E.; Lonie, D. C.; Vandermeersch, T.; Zurek, E.; Hutchison, G. R. *J. Cheminf.* **2012**, *4*, 17.

(42) Svergun, D. I. *J. Appl. Crystallogr.* **1992**, *25*, 495.

(43) Marcus, R. A. *J. Chem. Phys.* **1956**, *24*, 966.

(44) Marcus, R. A. *J. Chem. Phys.* **1965**, *43*, 679.

(45) Wu, L.; Liu, K.; Jie, J.; Song, D.; Su, H. *J. Am. Chem. Soc.* **2015**, *137*, 259.

(46) McGovern, D. A.; Quinn, S.; Doorley, G. W.; Whelan, A. M.; Ronayne, K. L.; Towrie, M.; Parker, A. W.; Kelly, J. M. *Chem. Commun.* **2007**, 5158.

(47) Peng, C. S.; Jones, K. C.; Tokmakoff, A. *J. Am. Chem. Soc.* **2011**, *133*, 15650.

(48) Closs, G. L.; Forbes, M. D. E.; Norris, J. R. *J. Phys. Chem.* **1987**, *91*, 3592.

(49) Hore, P. J.; Hunter, D. A.; Mckie, C. D.; Hoff, A. J. *Chem. Phys. Lett.* **1987**, *137*, 495.

(50) Weiss, E. A.; Ratner, M. A.; Wasielewski, M. R. *J. Phys. Chem. A* **2003**, *107*, 3639.

(51) Wiederrecht, G. P.; Svec, W. A.; Wasielewski, M. R. *J. Am. Chem. Soc.* **1999**, *121*, 7726.

(52) Hore, P. J. In *Advanced EPR in Biology and Biochemistry*; Hoff, A. J., Ed.; Elsevier: Amsterdam, 1989; p 405.

(53) Sinks, L. E.; Weiss, E. A.; Giaimo, J. M.; Wasielewski, M. R. *Chem. Phys. Lett.* **2005**, *404*, 244.

(54) Scott, A. M.; Miura, T.; Ricks, A. B.; Dance, Z. E. X.; Giacobbe, E. M.; Colvin, M. T.; Wasielewski, M. R. *J. Am. Chem. Soc.* **2009**, *131*, 17655.

(55) Miura, T.; Scott, A. M.; Wasielewski, M. R. *J. Phys. Chem. C* **2010**, *114*, 20370.